THE JOURNAL OF PHYSICAL CHEMISTRY C
A JOURNAL OF THE AMERICAN CHEMICAL SOCIETY

pubs.acs.org/JPCC

Article

Effect of Nitrogen Doping and Oxidation of Graphene on the Deposition of Platinum from Trimethyl(methylcyclopentadienyl)platinum(IV)

Ian E. Campbell, Nadire Nayir, Adri C. T. van Duin, and Suzanne E. Mohney*

Cite This: J. Phys. Chem. C 2022, 126, 16357−16368

Read Online

ACCESS | Metrics & More | Article Recommendations

ABSTRACT: Materials composed of nitrogen-doped carbon are useful as catalyst supports due to their low cost, low density, and enhanced metal−support interaction. One way to synthesize catalytic single atoms and nuclei on these supports is via vapor phase deposition processes. Here, density functional theory (DFT) was used to evaluate the effects of N doping and oxidation of graphene on the adsorption and dissociation of trimethyl(methylcyclopentadienyl) platinum ($MeCpPtMe_3$), which is a commonly used precursor in vapor deposition of platinum. DFT calculations confirmed that oxygen incorporation into graphene via oxidation of vacancies is thermodynamically favorable with and without N dopants. N doping was found to elongate substrate−oxygen bonds, thereby enhancing the interaction between $MeCpPtMe_3$ and oxidized defective graphene. According to nudged elastic band calculations, $MeCpPtMe_3$ dissociation on all oxidized substrates, with or without N doping, displayed positive enthalpies of reaction and activation energies. However, N doping drives the reactions by lowering the enthalpy of reaction and activation energy for the dissociation of $MeCpPtMe_3$ and the enthalpy of reaction for the subsequent chemisorption of $MeCpPtMe_2$, which was exothermic in all cases. Finally, the entire reaction beginning with $MeCpPtMe_3$ and two unreacted oxidized monovacancies and ending with $MeCpPtMe_2$ and a methyl group each bound to an oxidized monovacancy is exothermic for substrates containing pyridinic-*N* dopants.

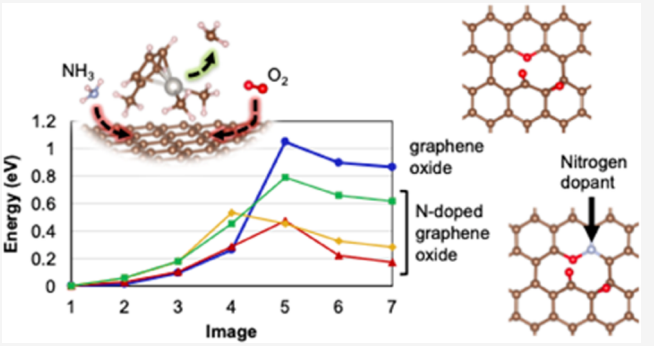

INTRODUCTION

Porous carbon-based materials are widely used as supports for catalysts due to their low cost, recyclability, and low density.[1−5] However, as catalyst support, porous carbon suffers from weak interactions with its host material and so metals supported by porous carbons tend to detach and agglomerate under working conditions.[6] A generally accepted solution to this problem is to utilize nitrogen-doped carbon as a substrate, which can reduce detachment and agglomeration of metals under working conditions by strengthening the metal−support interaction,[1,6,7] making nitrogen-doped carbon a promising substrate for catalytically active metals.[8]

One of the most studied catalytic materials is platinum, as it is used in several commercially essential fields including controlling vehicle emissions, producing chemicals, and catalyzing fuel cell reactions.[9] Unfortunately, platinum and other useful noble metals are exceedingly rare, so it is necessary to use them as efficiently as possible by utilizing them in high-surface-area forms like nanoparticles,[10−12] ultrathin films,[13−16] and even single atoms.[17]

Atomic layer deposition (ALD) is a useful technique for depositing within tortuous substrates like porous carbons that are frequently used as catalyst supports.[18−20] Under ideal circumstances, an ALD cycle can deposit conformal layers that are single-atom thick by exposing a substrate to alternating, surface-saturating, and self-limiting reactions.[21] The first few ALD cycles are critical for the deposition of small amounts of material in the form of thin films, single atoms, and nanoparticles. In fact, the first ALD half-cycle must depend directly on the substrate's surface chemistry. Additionally, many ALD processes display dependencies on substrate chemistry beyond the first few cycles in the form of nucleation delays, substrate-dependent growth modes[21,22] and conformality,[23] and area selectivity.[24]

Therefore, understanding and controlling substrate surface chemistry are essential for designing materials with the desired particle size and nucleation density and for addressing the issue

Received: June 14, 2022
Revised: September 7, 2022
Published: September 20, 2022

of nucleation delays. Oxygen-containing functional groups are among the most relevant and impactful of these surface species due to the presence of oxygen in the atmosphere.

Precursors such as trimethyl(methylcyclopentadienyl)-platinum ($MeCpPtMe_3$) decompose spontaneously in the presence of reactive oxygen-bearing species, which may be introduced into vapor deposition reactions as a coreactant[25] or through oxygen-containing functional groups on the substrate.[14,26] Initiating ALD on graphene has been the subject of several studies involving treatment with water, ozone, 3,4,9,10-perylene tetracarboxylic acid, molecular oxygen, NO_2, and oxygen plasma or coating of graphene surfaces with oxygen-containing materials like ZnO, HfO_2, Al_2O_3, and SiO_2.[27] Additionally, converting graphene to graphene oxide has been used as a strategy to enhance the nucleation of atomic layer deposited films.[27]

Oxidized carbon and nitrogen are known inclusions in N-doped graphene substrates.[28,29] Due to the enhanced nucleation and precursor decomposition resulting from oxygen-containing surface groups and the increased metal−substrate binding energy associated with N-doped substrates, it seems that oxidized nitrogen groups in carbon substrates could play an important role in initiating ALD reactions. Understanding and controlling substrate surface chemistry is essential for designing materials with the desired nuclei size and population density, which has motivated studies to seek atomic-level insight into the interaction between metal−organic precursors and their substrates. In particular, platinum-based metal−organic compounds are of great interest due to the usefulness and maturity of platinum chemistry. For these reasons, theoretical studies have been conducted to examine the physisorption, chemisorption, and reaction pathways of metal−organic platinum precursors on a variety of substrates, including silica,[30,31] nickel oxide,[32] and graphene;[14,33−35] interactions between platinum and undoped[36−39] and doped[7,39−43] graphene have been explored extensively using first-principles calculations. However, to the best of the authors' knowledge, the interplay between nitrogen doping and oxidized defects in graphene as well as platinum metal−organic precursors has not been investigated despite the relevance of all components involved. Here, we present first-principles calculations to probe the N-doping-assisted ALD surface reactions that occur during the first half-reaction between $MeCpPtMe_3$ and oxidized graphene.

METHODS

Using density functional theory (DFT), the thermodynamic favorability and chemical structure of oxidized monovacancies in nitrogen-doped graphene were explored. The adsorption of $MeCpPtMe_3$, the dissociation of $MeCpPtMe_3$ to form $MeCpPtMe_2$, and the adsorption of $MeCpPtMe_2$ are studied for different nitrogen-doping configurations in defective, oxidized graphene substrates. The progression of these calculations is illustrated in Figure 1.

DFT calculations were performed using the plane wave (PWscf) code of Quantum ESPRESSO.[44] Pseudopotentials, based on the generalized gradient approximation (GGA) and the Perdew, Burke, and Ernzerhof (PBE) exchange−correlation, from the standard solid-state pseudopotential library (SSSP, version 1.1.2) were employed.[45−49] Since this system was somewhat large and computationally expensive, did not require certain postprocessing steps, and featured molecular chemistry where the periodic nature of the simulation cell was not a main concern, a single k-point (γ) was used. The van der Waals

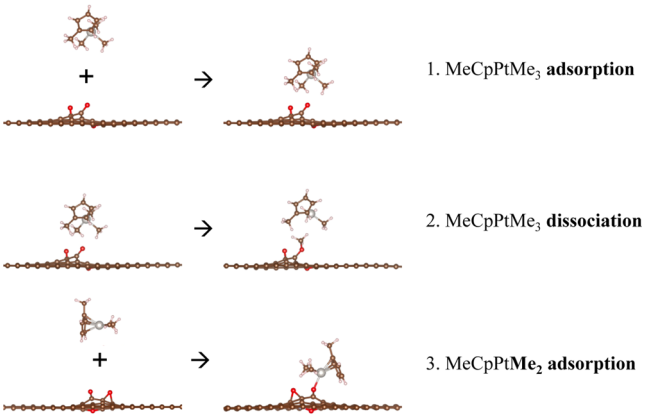

Figure 1. Schematic outlining the major calculations performed in this study. The adsorption reaction of the intact $MeCpPtMe_3$ precursor on various substrates was assessed in the first step. Then, the dissociation of $MeCpPtMe_3$ via transference of a methyl group to the substrate was examined. Finally, the adsorption reaction of $MeCpPtMe_2$, a product of the methyl transfer reaction, was investigated.

correction of Grimme (zero-damping DFT-D3)[50] was also utilized. Other parameters include Gaussian smearing with a degauss value of 0.01, a kinetic energy cutoff of 85 Ry (ecutwfc), and a charge density cutoff of 340 Ry (ecutrho). These values were chosen by performing convergence tests and choosing the first value that resulted in less than 0.0001% change from the previous value. An 8 × 8 periodic supercell of graphene (lattice parameter = 2.47 Å) was used in all calculations, and a vacuum with a height of 21.17 Å (40 Bohr radii) was inserted perpendicular to the plane of the graphene. Four representative substrates were considered to evaluate the effects of oxidation on substrate structure and precursor−substrate interactions: pristine, monovacant (MV) graphene, and two models containing monovacancies oxidized with two (MV + 2O) and three oxygen atoms (MV + 3O) inspired by Kaloni et al.[51] Structures with MV and an N dopant were constructed by removing two carbon atoms and replacing one with a N atom. Figure 2a depicts an MV + 3O structure with a single N dopant. N atoms were added at sites C1−C6 and at C13, as labeled in Figure 2b, where C represents a lattice site of graphene. A naming convention was used where a N atom at C1 or C2 is represented as N@C1 or N@C2 and so forth for all doping configurations. Chemical bonds were referred to using a notation with C1−O1 representing the bond between carbon atom C1 and oxygen atom O1 unless C1 was substituted for N, in which case the bond was called N1−O1. A close-up view of the vapor deposition precursor molecule, $MeCpPtMe_3$, considered with these substrates is shown in Figure 2c.

The oxidation energy, E_{ox}, for a graphene sheet with MV is defined as

$$E_{ox} = E_{MV+nO} - E_{MV} - (n/2)E_{O_2}$$

where E_{MV+nO} is the total energy of a free-standing relaxed graphene layer containing n number of O atoms, E_{MV} is the total energy of a relaxed graphene sheet with an unoxidized monovacancy, and E_{O_2} is the total energy of a diatomic triplet-state oxygen molecule in a vacuum. Percent bond length difference for all C−O and N−O bonds in MV + 2O and MV + 3O sheets was determined using the following equation

https://doi.org/10.1021/acs.jpcc.2c04117
J. Phys. Chem. C 2022, 126, 16357−16368

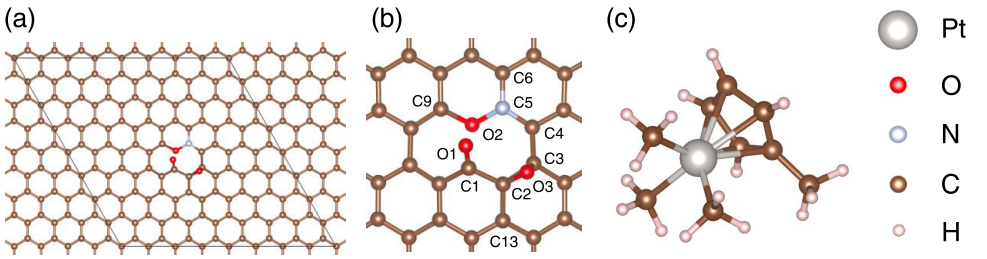

Figure 2. Full-scale (a) and cropped (b) ball-and-stick illustrations of a N-doped monolayer graphene sheet containing a divacancy oxidized by three oxygen atoms. The thin black line in (a) indicates the periodic supercell boundary. This structure is called MV + 3O with N@C5 referencing the presence of an N dopant at position C5. The structure called MV + 2O is similar to MV + 3O but is missing the atom labeled O3. $MeCpPtMe_3$ molecule (c).

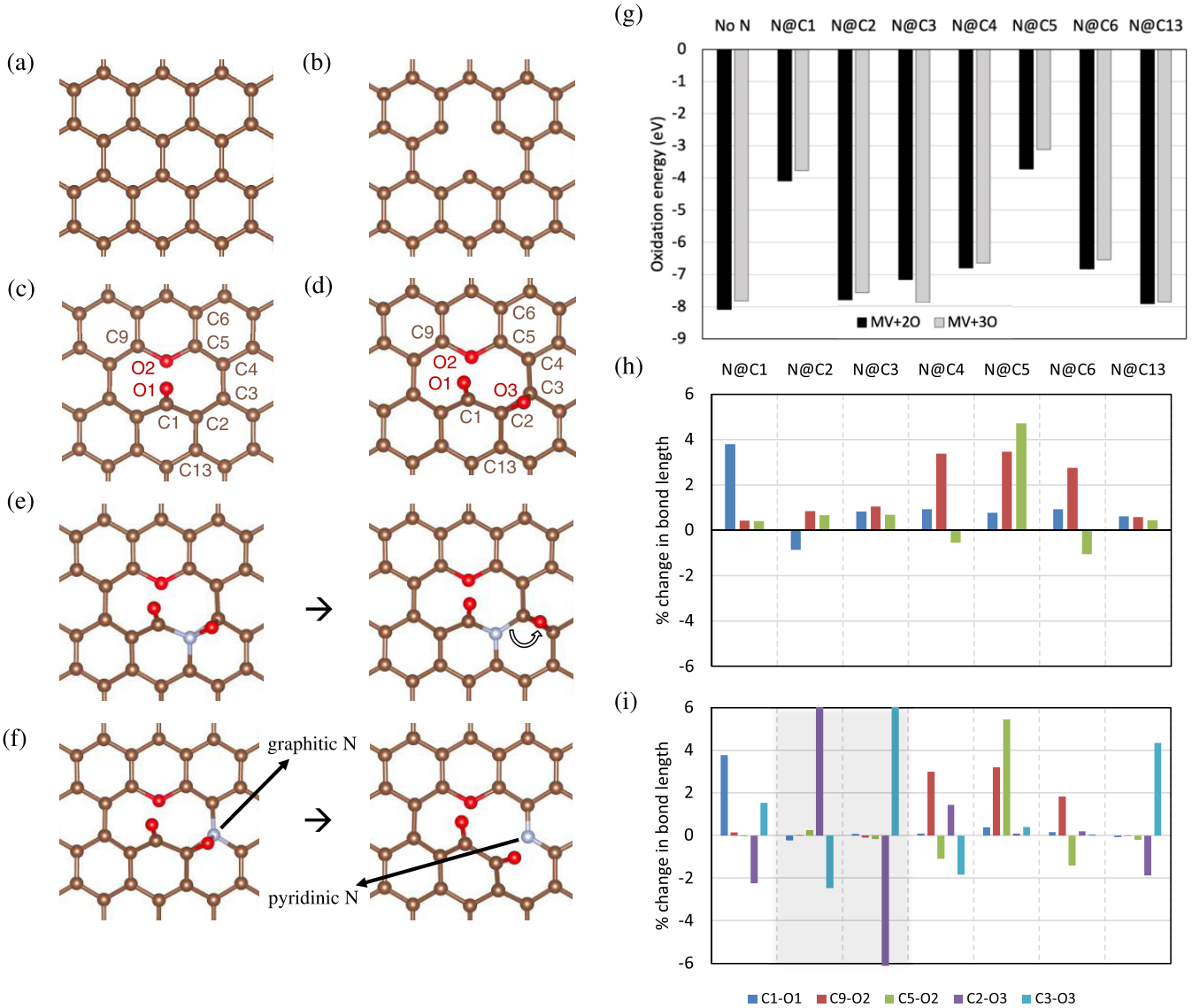

Figure 3. Relaxed pristine sheet (a), MV (b), MV + 2O (c), and MV + 3O substrates (d). MV + 3O with N@C2 (e) and N@C3 (f) models that experienced bond breakage upon relaxation. Initial and relaxed structures are to the left and right, respectively. The epoxide in MV + 3O with N@C2 has moved to the right so that it no longer incorporates the N dopant (a hollow arrow has been added to show the displacement of the O atom). The N−O and one N−C bond in MV + 3O with N@C3 broke such that pyridinic-*N* and carbonyl groups were formed (labels have been added to emphasize the change in the N type). Oxidation energies for undoped MV models and MV + 2O and MV + 3O models with single N substitutions (g). The locations of N substitutions are indicated by N@C# labels, e.g., the N@C1 structure has a N atom substituted for C1, as designated in Figure 2. Percent length changes for all bonds containing oxygen atoms in MV + 2O (h) and MV + 3O (i).

https://doi.org/10.1021/acs.jpcc.2c04117
J. Phys. Chem. C 2022, 126, 16357−16368

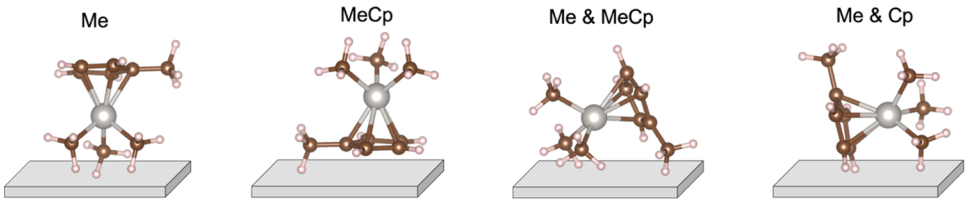

Figure 4. Four adsorption orientations of $MeCpPtMe_3$ on graphene adopted in the calculations. The gray slab represents the graphene substrates with/without defects and N and O inclusions.

$$\%\ \text{length change} = ((BL_{\text{N-doped}} - BL_{\text{no N}})/BL_{\text{no N}}) \times 100\%$$

where $BL_{\text{N-doped}}$ and $BL_{\text{no N}}$ represent the lengths of a specific bond in the N-doped and nondoped graphene structures, respectively. Positive (negative) percent changes indicate bond lengthening (shortening) because of N doping. Adsorption energies were defined as

$$E_{\text{ad}} = E_{\text{subs+MeCpPtMe}_3} - E_{\text{subs}} - E_{\text{MeCpPtMe}_3}$$

where $E_{\text{subs+MeCpPtMe}_3}$ is the total energy of a relaxed structure containing an $MeCpPtMe_3$ molecule adsorbed to the substrate, E_{subs} is the energy of the relaxed substrate on its own, and E_{MeCpPtMe_3} is the energy of a relaxed $MeCpPtMe_3$ molecule.

For electron density difference plots, two structures were relaxed. Each relaxed structure contained the same graphene substrate and an adsorbed or desorbed $MeCpPtMe_3$ molecule. The adsorbed $MeCpPtMe_3$ molecule was initially placed ~1.8 Å away from the nearest atoms in the unoxidized and oxidized graphene surfaces, respectively, whereas the desorbed $MeCpPtMe_3$ molecule was positioned ~8.5 Å away from the surface. These structures were then processed with self-consistent field (SCF) calculations, and the postprocessing (pp.x) features of Quantum ESPRESSO[44] were utilized to generate electron densities for each structure. Finally, the electron densities were subtracted from one another to visualize the effect of $MeCpPtMe_3$ on electron distribution in the substrates. The nudged elastic band (NEB) method[52] was deployed to assess the reaction pathway of methyl transfer from an adsorbed $MeCpPtMe_3$ molecule to multiple oxidized substrates. Energy cutoffs, smearing parameters, and van der Waals correction for the NEB calculations were kept the same as for the structural relaxations. All of the studied structures were visualized using VESTA.[53]

RESULTS AND DISCUSSION

O- and N-Doping Effect. First-principles calculations were performed to uncover the interplay between N- and O-functional groups in graphene and the surface reactivity of graphene. Figure 3 presents the four representative models adopted in this study, namely, pristine (Figure 3a), MV (Figure 3b), MV + 2O (Figure 3c), and MV + 3O (Figure 3d). N-doped MV + 2O and MV + 3O structures were found to be stable upon structural relaxation except for the MV + 3O structures with N@C2 (Figure 3e) and N@C3 (Figure 3f), which experienced bond breakage during structural relaxation. E_{ox} for N-functionalized MV + 2O and MV + 3O models is plotted in Figure 3g. $E_{\text{ox}} < 0$ indicates an energetically favored reaction.

According to Figure 3g, oxidation on all sheets containing vacancies is exothermic ($E_{\text{ox}} < 0$), meaning that the formation of oxidized monovacancies in undoped and N-doped graphene substrates is thermodynamically viable. E_{ox} is more negative for MV + 2O than that for MV + 3O for all structures except those with N@C3, which is likely caused by the bond breakage that occurred in MV + 3O with N@C3 during structural relaxation (Figure 3f). All substrates with N@C1 and N@C5 have noticeably less negative E_{ox} than the other doping configurations, likely due to the formation of N−O bonds, which are weaker than C−O bonds.[54] The percent changes in C−O bond lengths and the lengths of N−O bonds they are replaced by are plotted in Figure 3h,i. With N@C1, the N1−O1 bond in MV + 3O and MV + 2O was found to be ~3.8% longer than the corresponding C1−O1 bonds. Additionally, doping by N@C5 caused C9−O2 and C5−O2 to lengthen considerably and N@C6 caused similar but less intense lengthening of C9−O2. N@C13 caused almost no change for MV + 2O but caused substantial lengthening of C3−O3 of more than 4%. The noticeable lengthening of C1−O1, C5−O2, and C9−O2 bonds coupled with more positive E_{ox} due to N doping indicates increased reactivity for O atoms bound to N-doped substrates, especially those containing N−O bonds. Increased substrate reactivity would likely impact key reactions like the combustion of precursor ligands or their dissociation on the substrate surface.

Due to bond scission upon the structural relaxation of MV + 3O with N@C2 (Figure 3e) and N@C3 (Figure 3f), percent changes are grayed out for these structures (Figure 3i), and it should be noted that the scaling excludes the full range of values observed for these configurations. Specifically, the C2−O3 interatomic distance increased by 67.9% and decreased by 14.6% for N@C2 and N@C3, respectively, and the C3−O3 interatomic distance increased by 92.3% for N@C3. The drastic changes in interatomic distance, corresponding to N@C2 doping in MV + 3O, are due to the migration of the O3 oxygen atom during structural relaxation (Figure 3e). The nitrogen-containing epoxide in the final structure of MV + 3O with N@C2 includes the carbon atom that was present in the initial epoxide, but the O atom is no longer bound to N. Similarly, the epoxide in the MV + 3O structure with N@C3 (Figure 3f) was severed, but a carbonyl group containing O and C from the initial epoxide structure was formed, indicating that the formation of pyridinic and carbonyl groups is more energetically favorable than migration of the O atom for this particular case. A decrease of 2.5% was observed for C3−O3 in MV + 3O with N@C2 since this bond was not broken but was incorporated into a C−O−C bonding configuration instead of the initial N−O−C configuration. Otherwise, N@C2 and N@C3 cause small bond length changes $\lesssim$1% for both MV + 2O and MV + 3O. It is worth noting that, due to MV + 3O with N@C2 and N@C3 having altered bonding configurations, these structures were not considered in the final analysis.

In the interest of reducing computational cost and eliminating uninteresting cases, N@C1, N@C5, and N@C13 were chosen

https://doi.org/10.1021/acs.jpcc.2c04117
J. Phys. Chem. C 2022, 126, 16357−16368

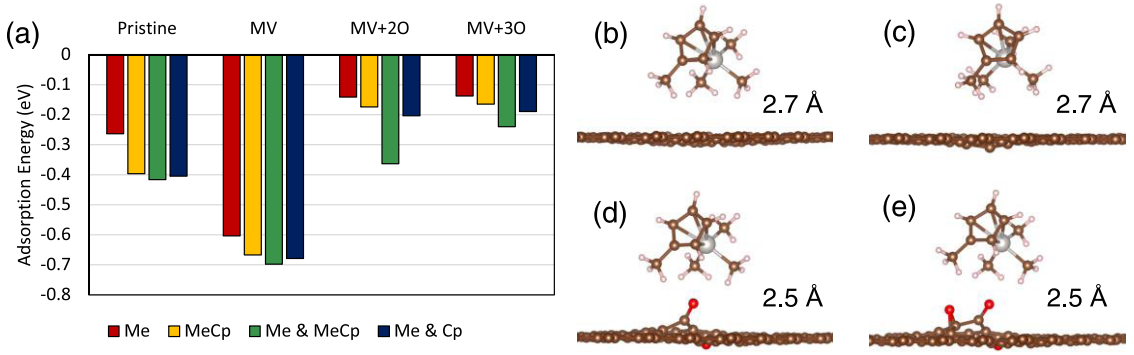

Figure 5. Bar chart depicting adsorption energies of $MeCpPtMe_3$ in four orientations on four different graphene-based substrates (a). Ball-and-stick structures depicting relaxed geometries of $MeCpPtMe_3$ adsorbed onto pristine (b), monovacant (c), MV + 2O (d), and MV + 3O (e) substrates in the Me and MeCp orientation. The distances in (b)−(e) are the smallest measured between an atom in the $MeCpPtMe_3$ molecule and an atom on the substrate.

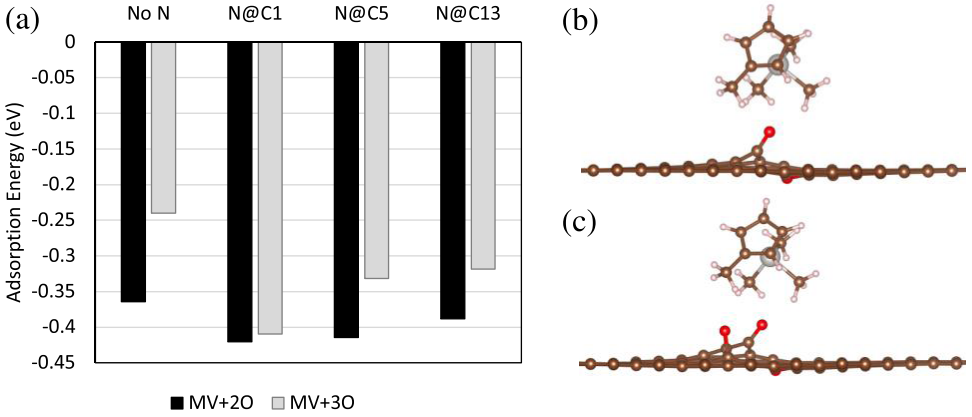

Figure 6. Plot showing adsorption energies for $MeCpPtMe_3$ in the Me and MeCp orientation on MV + 2O and MV + 3O with no N and DV + 2O and DV + 3O with N@C1, N@C5, and N@C13 doping configurations (a). Visualizations of relaxed structures wherein $MeCpPtMe_3$ is adsorbed to undoped MV + 2O (b) and MV + 3O (c) substrates.

for $MeCpPtMe_3$ adsorption and dissociation analysis due to the implied reactivity increase for a different O atom in each doping configuration: O1 in N@C1, O2 in N@C5, and O3 in N@C13.

Precursor Binding. Multiple $MeCpPtMe_3$ adsorption orientations were tested on pristine graphene and substrates with MV and oxidized MV with and without N doping. The E_{ad} was calculated for the four $MeCpPtMe_3$ orientations shown in Figure 4, where the precursor−substrate interaction is governed by a different set of ligands for each orientation: all three methyl ligands in "Me", the methylcyclopentadienyl (MeCp) group coplanar to the substrate in "MeCp", two methyl ligands and the methyl group from the MeCp ligand in "Me and MeCp", and two methyl ligands and the ring from the MeCp ligand in an edge-on orientation in "Me and Cp". The E_{ad} is reported for relaxed structures (Figure 5a) containing each of these orientations on pristine (Figure 5b), MV (Figure 5c) and undoped MV + 2O (Figure 5d) and MV + 3O (Figure 5e) substrates. Note that $E_{ad} < 0$ indicates an energetically favored reaction.

No dissociation of the precursor or substrate bonds was observed in any of the relaxed structures. As depicted in Figure 5, the Me and MeCp orientation is the most thermodynamically stable orientation upon adsorption of $MeCpPtMe_3$. Additionally, E_{ad} is the lowest for the MV substrate due to the presence of C-dangling bonds near the defect. The next lowest E_{ad} is found for the pristine case and then both oxidized monovacancies that showed comparable E_{ad}. Oxidized MV substrates may have higher E_{ad} than the pristine substrate due to a larger separation between the adsorbed $MeCpPtMe_3$ molecule and the carbon atoms in the graphene sheet, which was added to make room for the O atoms. The separation between the precursor molecule and the graphene surface is ∼2.7 Å for the pristine and monovacancy cases, ∼3.1 Å for MV + 2O, and ∼3.3 Å for MV + 3O. For the unoxidized graphene sheets, $MeCpPtMe_3$ may be interacting with many C atoms as opposed to just one or two O atoms in the oxidized substrates, which might account for the less negative E_{ad} for $MeCpPtMe_3$ adsorption on MV + 2O and MV + 3O.

Utilizing the most thermodynamically stable adsorption configuration (Me and MeCp), the impact of nitrogen doping on the adsorption energy of $MeCpPtMe_3$ on oxidized MV models with no N, N@C1, N@C5, and N@C13 was investigated. Oxidized MV models were used over bare MV models, as oxidation of MV was found to be energetically favorable. According to Figure 6a, MV + 2O still results in the more negative adsorption energy (E_{ad}) compared to MV + 3O for doped and undoped structures. The adsorption energy for the doped structures is consistently more negative compared to those for the undoped structures, indicating that nitrogen doping strengthens the interaction between the oxidized substrate and the physiosorbed $MeCpPtMe_3$ molecule, similarly to how N doping strengthens the interaction between platinum

https://doi.org/10.1021/acs.jpcc.2c04117
J. Phys. Chem. C 2022, 126, 16357−16368

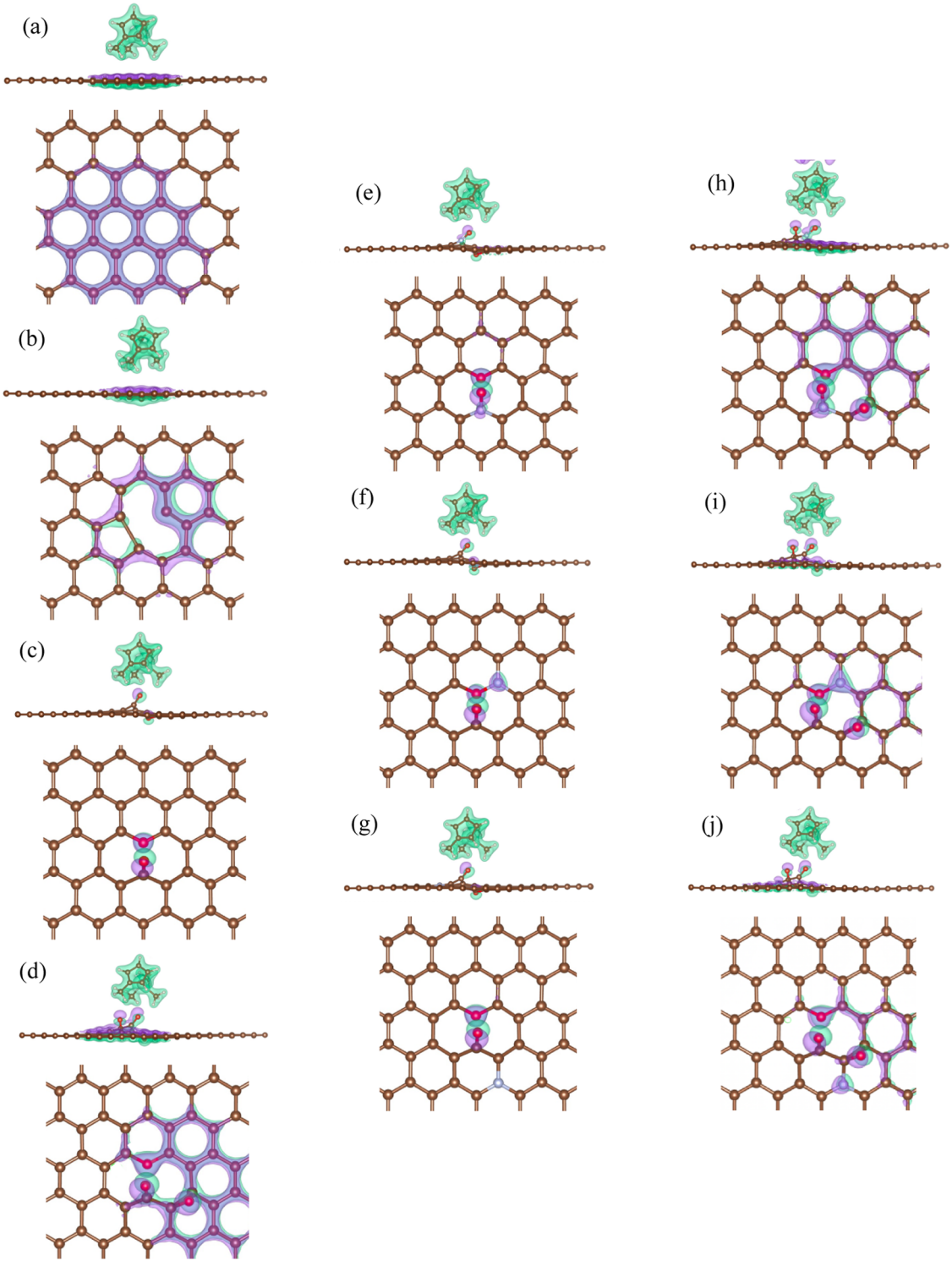

Figure 7. Electron density difference isosurfaces (cutoff = 0.075 a_0^{-3}) for pristine (a), MV (b), MV + 2O (c), MV + 3O (d), MV + 2O with N@C1 (e), MV + 2O with N@C5 (f), MV + 2O with N@C13 (g), MV + 3O with N@C1 (h), MV + 3O with N@C5 (i), and MV + 3O with N@C13 (j) substrates calculated for the adsorption of a $MeCpPtMe_3$ molecule to each substrate. Green (light) and purple (dark) isosurfaces represent positive and negative changes in electron density, respectively, coinciding with adsorption of the $MeCpPtMe_3$ molecule in the Me and MeCp orientation. The displayed geometry data (ball-and-stick models) depict each structure after the adsorption of an $MeCpPtMe_3$ molecule.

metal and carbon substrates.[1,6,7] The increase in interaction strength is likely due to the weakening of substrate−oxygen bonds via N doping, which was confirmed by bond length measurements displayed in Figure 3h,i. Interestingly, there is a relatively large difference between adsorption energies for the undoped MV + 2O and MV + 3O structures but almost no difference in adsorption energy for these structures for N@C1 doping. This unequal response to N doping may be explained by the noticeable changes in O3 bonds upon adding N@C1 in MV + 3O since the changes in bonds to O1 and O2 are nearly the same for MV + 2O and MV + 3O (Figure 3h,i). Figure 6b,c

https://doi.org/10.1021/acs.jpcc.2c04117
J. Phys. Chem. C 2022, 126, 16357−16368

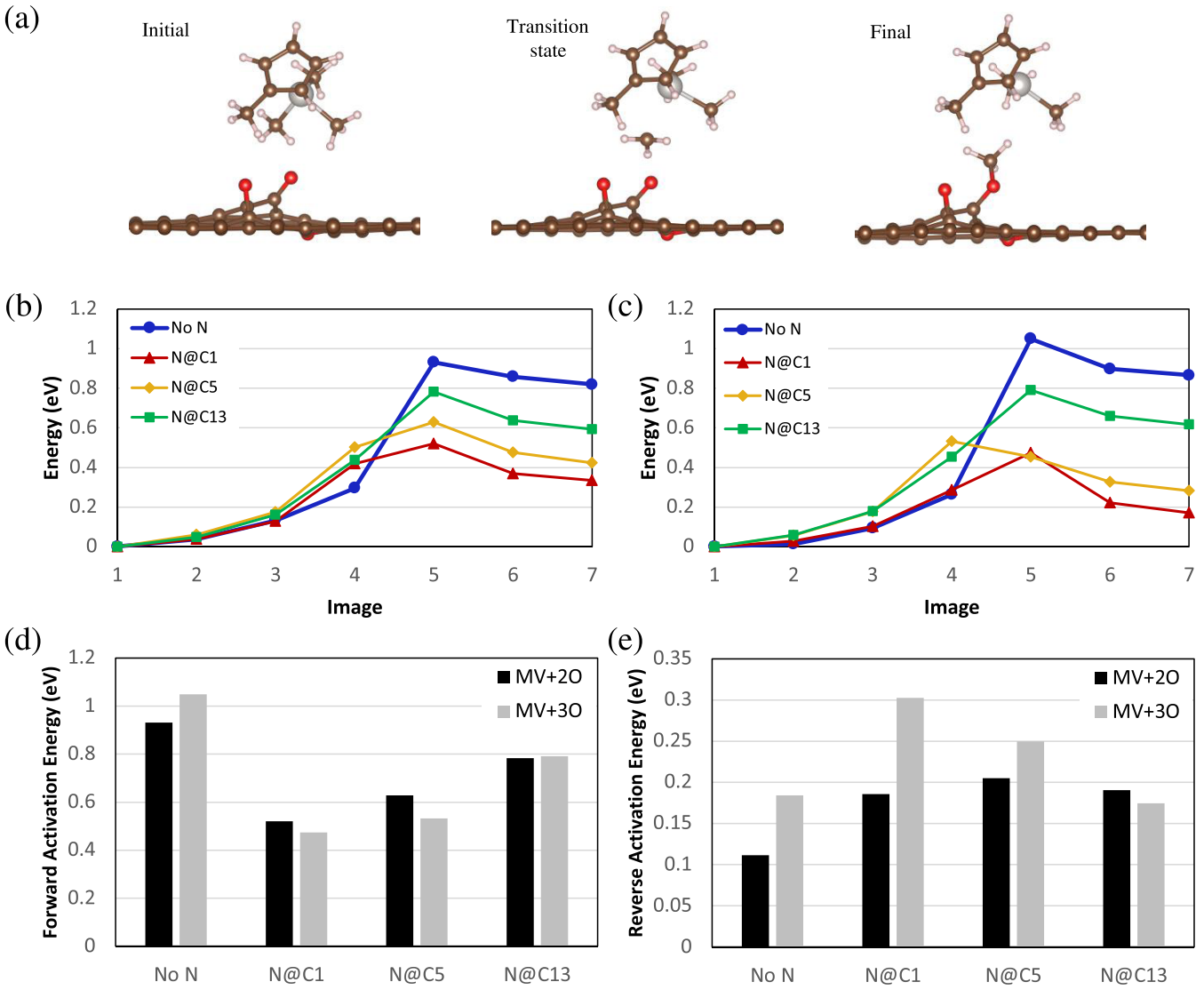

Figure 8. Example of initial, final, and transition-state structures generated by NEB calculations for methyl transfer from $MeCpPtMe_3$ to O1 in the MV + 3O structure (a). Plotted energies from NEB calculations for MV + 2O structures with no N, N@C1, N@C5, and N@C13 (b) and MV + 3O structures with no N, N@C1, N@C5, and N@C13 (c). Images one and seven correspond to the initial and final states, respectively, and the image with the highest energy is the transition state. Activation energies for the forward (d) and reverse (e) methyl transfer reactions on MV + 2O and MV + 3O structures with no N, N@C1, N@C5, and N@C13 were calculated by subtracting the initial and final energies from the transition-state energy.

depicts the relaxed structures wherein $MeCpPtMe_3$ is adsorbed on undoped MV + 2O and MV + 3O substrates, respectively.

Electron Density Difference. Electron density difference plots generated for pristine, MV, MV + 2O, and MV + 3O structures are displayed in Figure 7a–d, the plots for MV + 2O with N@C1, N@C5, and N@C13 are shown in Figure 7e–g, and those for MV + 3O with N@C1, N@C5, and N@C13 are shown in Figure 7h–j, respectively. Overall, an increase in electron density was observed on the side of the graphene sheet opposite the $MeCpPtMe_3$ molecule, indicating flexion away from the molecule. Local bending of each sheet away from the $MeCpPtMe_3$ molecule can be observed in the ball-and-stick models in Figure 7. Note that electron density changes in the graphene of the doped and undoped MV + 2O models (Figure 7c,e–g) occurred but are not visible due to the isosurface cutoff (0.075 a_0^{-3} (a_0 = Bohr radius)). The electron density of all oxygen atoms adsorbed to graphene substrates is shifted upon adsorption, indicating an interaction between them and the adsorbed $MeCpPtMe_3$ molecule. The electron density shift in the graphene sheet of the MV + 3O structures (Figure 7d,h–j) is much more pronounced than that observed in the MV + 2O structures, but electron density shifts on the O atoms themselves are very similar in both structures.

Electron density difference plots for MV + O2 and MV + O3 models with N@C1, N@C5, and N@C13 show that electron density changes due to $MeCpPtMe_3$ adsorption on doped MV + 2O and MV + 3O are also more pronounced around N atoms relative to the surrounding graphene sheet. The increased polarizability of electrons near N dopants could help explain the fact that adsorption energies for $MeCpPtMe_3$ are lower for all N-doped substrates than those for undoped substrates, as shown in Figure 7. N@C1 in MV + 2O (Figure 7e) apparently allowed for electron density changes at the edge of the MV defect and immediately adjacent to the O1 atom with which the $MeCpPtMe_3$ molecule predominantly interacted. N@C5 in MV + 2O (Figure 7f) caused a similar effect but was adjacent to O2, which does not extend in the z-direction toward the $MeCpPtMe_3$ molecule. N@C13 in MV + 2O (Figure 7g) shows

https://doi.org/10.1021/acs.jpcc.2c04117
J. Phys. Chem. C 2022, 126, 16357−16368

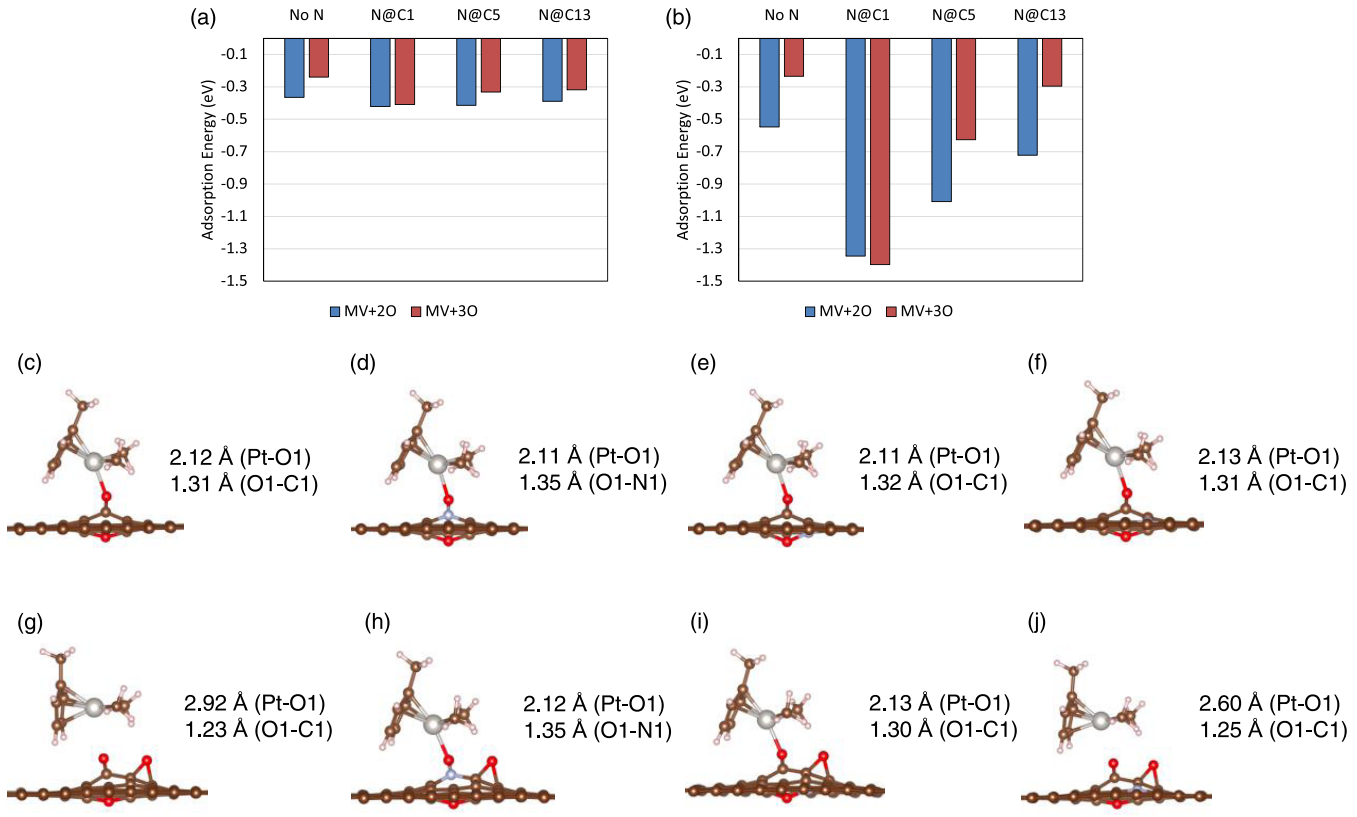

Figure 9. Rescaled adsorption energies for $MeCpPtMe_3$ on doped and undoped MV + 2O and MV + 3O substrates from Figure 6 for comparison (a). Adsorption energies for $MeCpPtMe_2$ on doped and undoped MV + 2O and MV + 3O substrates (b). Relaxed structures for $MeCpPtMe_2$ molecules initially placed ~1.8 Å away from MV + 2O with no N (c), MV + 2O with N@C1 (d), MV + 2O with N@C5 (e), MV + 2O with N@C13 (f), MV + 3O with no N (g), MV + 3O with N@C1 (h), MV + 3O with N@C5 (i), and MV + 3O with N@C13 (j). Numbers listed for (c)−(j) are interatomic distances between Pt and O1 and between O1 and C1 (for N@C5 and N@C13) or N1 (for N@C1).

no change in electron density for this isosurface cutoff and is not located at the edge of the MV. These qualitative differences between N dopants help to rationalize the decrease in adsorption energy from N@C1 to N@C5 to N@C13, as shown in Figure 6a. Very similar effects can be observed in the N-doped MV + 3O structures (Figure 7h−j). Except electron density changes are apparent around N@C13 in MV + 3O (Figure 7j) for this isosurface cutoff, although the colored regions around N@C5 in MV + 3O are noticeably larger than those around N@C13 in MV + 3O, indicating the weaker effect of this doping configuration on E_{ad}.

Nudged Elastic Band Calculations. NEB calculations were performed to analyze reaction pathways for methyl transfer from the $MeCpPtMe_3$ molecule to O1 in oxidized MV structures relative to N doping. The Me and MeCp orientation was chosen because it has the most negative adsorption energy for all tested substrates and orientations. In reality, there are many orientations from which the dissociation of an adsorbed $MeCpPtMe_3$ molecule could initiate. O1 was chosen due to its proximity to the precursor molecule relative to O2 and the fact that it is directly bound to the monovacancy, whereas O3 is not. The dissociation of a methyl group was chosen as a case study reaction to reduce the complexity in the calculations and because the energetic favorability of Me instead of MeCp dissociating from $MeCpPtMe_3$ has been established in the literature.[26,33,55] The $MeCpPtMe_2$ fragment is not bound to the substrate in the final state of these NEB calculations due to the lack of reactive surface species near the $MeCpPtMe_2$ fragment after methyl transfer. It should be noted that concerted $MeCpPtMe_2$ chemisorption might occur on a more realistic substrate, which could include more reactive sites on the substrate surface in the form of larger or more plentiful oxidized vacancies. However, such increased complexity might also complicate or obfuscate conclusions drawn about the effects of N doping on substrate reactivity. Additionally, Karasulu et al.[14] found that $MeCpPtMe_3$ dissociating over pristine graphene likely proceeds by the dissociation of methyl ligands followed by the chemisorption of $MeCpPtMe_2$ through the undercoordinated Pt atom. In fact, $MeCpPtMe_2$ does not interact with pristine graphene through the Pt atom, indicating that free $MeCpPtMe_2$ is a possible byproduct of ligand transfer reactions when not in the presence of reactive functional groups. Therefore, chemisorption of $MeCpPtMe_2$ is considered later in this study on a separate, unreacted oxidized monovacancy, and the energetics of methyl transfer and $MeCpPtMe_2$ chemisorption are considered together in the final analysis.

Figure 8a depicts the initial, final, and transition states of this dissociation reaction for the MV + 3O substrate. Note that the methyl group closest to the O1 atom was chosen for the reaction. Normalized energies for each image of the NEB calculations are plotted in Figure 8b (MV + 2O with no N, N@C1, N@C5, and N@C13) and Figure 8c (MV + 3O with no N, N@C1, N@C5, and N@C13). Activation energies for the forward (Figure 8d) (and reverse (Figure 8e)) reactions were calculated by subtracting the total energy of the initial (and final) reaction state from that of the transition state. According to Figure 8b,c,

https://doi.org/10.1021/acs.jpcc.2c04117
J. Phys. Chem. C 2022, 126, 16357−16368

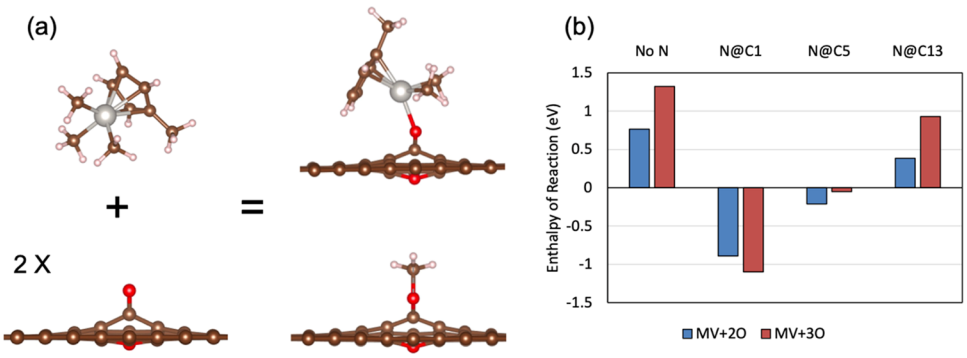

Figure 10. Schematic representation of the complete and balanced chemisorption reaction beginning with an intact $MeCpPtMe_3$ molecule and two identical substrates containing an oxidized monovacancy. The final state consists of $MeCpPtMe_2$ and a methyl ligand each bound to the O1 atom of separate, identical substrates (a). Enthalpies of reaction associated with the reaction depicted in (a) are shown in (b). Negative (positive) energies indicate an energetically favorable (unfavorable) reaction.

the methyl transfer is kinetically limited, and the enthalpy of reaction is positive (i.e., endothermic) in all cases.

The forward activation energy for the undoped MV + 2O structure is less than that for undoped MV + 3O. However, upon addition of N@C1 and N@C5, MV + 3O has the lower forward activation energy and the forward activation energy for MV + 2O is lower again with N@C13. N doping becomes more effective at lowering the forward activation for more highly oxidized structures and when the N dopant is closer to the vacancy, but all N-doping configurations lower the forward activation energy. More negative/less positive activation energy is associated with a faster rate of reaction.

N@C1 in MV + 2O and MV + 3O yields the lowest forward activation energies, which may be explained by electron deficiency induced in O1 by the replacement of C1 with more electronegative N. Removal of electron density from O1 would enhance the attraction between the O atom and CH_3 anion. Forward activation energies for the N@C5 structures are larger than those for N@C1 and those for N@C13 are larger still, demonstrating that pyridinic-*N* dopants cause the greatest reduction in activation energy for $MeCpPtMe_3$ dissociation at MV. Graphitic N dopants do not cause as intense an effect but still enhance the reactivity of nearby oxidized MV.

Finally, reverse activation energies for dissociation of the methyl group from the substrate and its subsequent attachment to $MeCpPtMe_2$ are the highest for N-doped substrates. MV + 3O has the highest reverse activation energy for N@C1, followed by N@C5, undoped, and N@C13, which is only slightly lower than undoped. The highest reverse activation energy for MV + 2O corresponds to N@C5, then N@C13, N@C1, and, at last, the undoped structure. Thus, methyl transfer to the substrate becomes less reversible for substrates with N dopants closer to the Me−O bond and for substrates with increased oxidation. Overall, the low forward activation energies, high reverse activation energies, and lower reaction enthalpies associated with $MeCpPtMe_3$ dissociation on N-doped substrates indicate that thermally activated dissociation of $MeCpPtMe_3$ would be enhanced for substrates that are more heavily N-doped.

Precursor Reactions after Methyl Dissociation. To investigate the progression of Pt deposition after the methyl dissociation reaction, adsorption energy calculations were performed for a $MeCpPtMe_2$ molecule initially placed ∼1.8 Å away from doped and undoped MV + 2O and MV + 3O structures, similar to the calculations represented in Figure 6. A rescaled version of Figure 6a is shown in Figure 9a for comparison to Figure 9b, which displays E_{ad} for $MeCpPtMe_2$ on MV + 2O and MV + 3O substrates. Note that the Me and Cp adsorption orientation was found to be most energetically favorable for $MeCpPtMe_2$, so this orientation was used for the calculations represented in Figure 9. E_{ad} is noticeably more negative for $MeCpPtMe_2$ on MV + 2O than $MeCpPtMe_3$ but is approximately the same for both molecules on MV + 3O, indicating enhanced energetic favorability for the chemisorption of $MeCpPtMe_2$ on MV + 2O but not MV + 3O. As expected, E_{ad} is more negative for $MeCpPtMe_2$ than $MeCpPtMe_3$ on MV + 2O and MV + 3O substrates with N@C1, N@C5, and N@C13, with the most intense changes observed for N@C1, then N@C5, and at last N@C13.

Key differences between $MeCpPtMe_2$ chemisorption reactions on differently doped substrates can also be observed in the visualized geometry data displayed in Figure 9c−f, which correspond to the relaxed structures of $MeCpPtMe_2$ on undoped MV + 2O, MV + 2O with N@C1, MV + 2O with N@C5, and MV + 2O with N@C13, respectively, and Figure 9g−j, which correspond to $MeCpPtMe_2$ on undoped MV + 3O and MV + 3O with N@C1, MV + 3O with N@C5, and MV + 3O with N@C13. Interatomic distance measurements for Pt−O1 and O1−C1 or O1−N1 pairs are also given in Figure 9c−j. The Pt atom in $MeCpPtMe_2$ can be seen flexing more intensely toward O1 for substrates yielding more negative E_{ad}. This flexion can be attributed to the formation of a bond between Pt and O1. Such bond formation was not observed for $MeCpPtMe_3$ on any substrate as the methyl groups occluded the approach of the Pt atom towards O1 and the distance between Pt and O1 in these cases was ∼3.8 to 4.0 Å. The distance between Pt and O1 for $MeCpPtMe_2$ adsorption calculations ranges from 2.11 to 2.92 Å.

The interatomic distance between Pt in $MeCpPtMe_2$ and O1 in MV + 2O varies slightly due to N doping, with Pt−O1 = 2.12 Å for MV + 2O with no N (Figure 9c), Pt−O1 = 2.11 Å for N@C1 (Figure 9d) and N@C5 (Figure 9e), and Pt−O1 = 2.13 Å for N@C13 (Figure 9f). $MeCpPtMe_2$ on MV + 3O with no N (Figure 9g) has a long Pt−O1 separation distance of 2.92 Å and shows little to no flexion of the precursor molecule toward the substrate. Such a long distance between Pt and O1 is not surprising for this structure, as it yielded the least negative E_{ad}. However, MV + 3O with N@C1 (Figure 9h) and N@C5 (Figure 9i) show lower Pt−O1 bond lengths of 2.12 and 2.13 Å, respectively. $MeCpPtMe_2$ on MV + 3O with N@C13 (Figure 9j) represents an intermediate case with Pt−O1 = 2.60 Å and

https://doi.org/10.1021/acs.jpcc.2c04117
J. Phys. Chem. C 2022, 126, 16357−16368

only moderate observable flexion of the $MeCpPtMe_2$ molecule. As expected, contraction of the distance between Pt and O1 causes the bonds between O1 and the substrate to lengthen. This can be observed in the overall inverse correlation between Pt−O1 and O1−C1 or O1−N1 separation distances listed in Figure 9.

Overall, E_{ads} calculations and bond length measurements indicate that N doping causes the formation of a bond between O1 in MV + 3O and the undercoordinated Pt atom in $MeCpPtMe_2$ in addition to strengthening the bond between O1 in MV + 2O and Pt in $MeCpPtMe_2$. The effects of N doping on the interaction between $MeCpPtMe_2$ and O1 are dependent on dopant type, with N@C1 producing the greatest effect followed by N@C5 then N@C13. Additionally, it is apparent that the precursor−substrate interaction is stronger for $MeCpPtMe_2$ than $MeCpPtMe_3$ on all doped substrates and on undoped MV + 2O.

Finally, the enthalpy was determined for the entire reaction beginning with a free $MeCpPtMe_3$ molecule and two identical substrates containing oxidized monovacancies then ending with $MeCpPtMe_2$ and CH_3 each bound to an identical substrate (Figure 10a). Enthalpies for this reaction on MV + 2O and MV + 3O substrates with N@C1, N@C5, and N@C13 are displayed in Figure 10b. MV + 2O and MV + 3O with no N and N@C13 gave positive enthalpies of reaction. However, the enthalpy of reaction is significantly lower for substrates with N@C13 than those with no N. N@C5 further lowers the enthalpy of reaction so that it becomes negative, meaning the reaction is energetically favored, and N@C1 produces a similar but even more pronounced effect. Thus, the endothermic reactions observed for methyl transfer with $MeCpPtMe_2$ remaining in the vapor phase (Figure 8) likely do not reflect the decomposition of $MeCpPtMe_3$ entirely accurately. More specifically, larger-scale density functional theory or molecular dynamics simulations containing more vacancies, different vacancy types, and/or more oxygen-containing functional groups per vacancy could allow for the study of more realistic $MeCpPtMe_3$ chemistry. However, these simplified calculations serve as a proof of concept and illustrate the important conclusions that the adsorption energy of $MeCpPtMe_3$ on oxidized graphene defects is enhanced by N doping, the dissociation of $MeCpPtMe_3$ is likely catalyzed by N dopants, and the chemisorption of $MeCpPtMe_2$ (and $MeCpPtMe_3$) can be made more energetically favorable by N dopants.

CONCLUSIONS

The impact of N doping on the reaction between $MeCpPtMe_3$ and oxygen atoms bound to monovacancies in graphene was assessed using density functional theory (DFT). It was determined that oxidation of monovacancies is exothermic for the case of N doping at pyridinic and graphitic sites and that N doping at specific locations changes the reactivity of O atoms bound to the monovacancy. In general, the inclusion of N dopants in oxidized graphene substrates enhanced the reactivity of the substrate toward the adsorption and dissociation of $MeCpPtMe_3$. N dopants in closer proximity to the monovacancy and oxygen atoms caused a greater effect than those farther away, and, in general, the presence of N−O bonds led to the most dramatic change in reactivity. Charge density difference plots showed increased variation in electron density directly at the site of N dopants and around the dopant atoms, possibly explaining the effect of N dopants on adsorption energy.

Nudged elastic band (NEB) calculations showed that N doping enhanced the reactivity of surface oxygen by reducing the forward kinetic barrier while making the reverse reaction less favorable. Doping site and N type (graphitic vs pyridinic) also have a critical effect on the dissociation reaction. Regardless of doping, methyl dissociation on oxidized graphene is endothermic and kinetically hindered, but N doping reduces the kinetic barrier and lowers the energy of the final state. By comparing adsorption energies of $MeCpPtMe_2$ and $MeCpPtMe_3$ on doped and undoped substrates, it was concluded that the initial methyl dissociation acts as a rate-limiting step in the surface reactions since methyl dissociation is followed by the energetically more favorable $MeCpPtMe_2$ adsorption reactions. Methyl dissociation and $MeCpPtMe_2$ adsorption are made even more energetically favorable by N doping and display dependence on dopant location. These findings pave the way for understanding and controlling the effects dopants have on vapor deposition reactions on widely used graphene-based substrates.

AUTHOR INFORMATION

Corresponding Author

Suzanne E. Mohney − *Department of Materials Science and Engineering, The Pennsylvania State University, University Park, Pennsylvania 16802, United States;* orcid.org/0000-0001-5649-7640; Phone: 814-863-0744; Email: mohney@psu.edu

Authors

Ian E. Campbell − *Department of Materials Science and Engineering, The Pennsylvania State University, University Park, Pennsylvania 16802, United States;* orcid.org/0000-0002-1988-0939

Nadire Nayir − *Department of Physics, Karamanoğlu Mehmetbey University, Karaman 70000, Turkey; 2D Crystal Consortium Material Innovation Platform (2DCC-MPI) Materials Research Institute, The Pennsylvania State University, University Park, Pennsylvania 16802, United States; Department of Mechanical Engineering, The Pennsylvania State University, University Park, Pennsylvania 16802, United States;* orcid.org/0000-0002-3621-2481

Adri C. T. van Duin − *Department of Mechanical Engineering, The Pennsylvania State University, University Park, Pennsylvania 16802, United States; 2D Crystal Consortium Material Innovation Platform (2DCC-MPI) Materials Research Institute, The Pennsylvania State University, University Park, Pennsylvania 16802, United States; Department of Materials Science and Engineering, The Pennsylvania State University, University Park, Pennsylvania 16802, United States;* orcid.org/0000-0002-3478-4945

Complete contact information is available at: https://pubs.acs.org/10.1021/acs.jpcc.2c04117

Notes

The authors declare no competing financial interest.

ACKNOWLEDGMENTS

Funding was provided by the National Science Foundation through the Pennsylvania State University MRSEC Program (DMR-1420620) and the Pennsylvania State University 2D Crystal Consortium−Materials Innovation Platform (2DCC-MIP) under NSF cooperative agreements DMR-1539916 and DMR-2039351.

REFERENCES

(1) Melke, J.; Schuster, R.; Möbus, S.; Jurzinsky, T.; Elsässer, P.; Heilemann, A.; Fischer, A. Electrochemical Stability of Silica Templated Polyaniline Derived Mesoporous N-Doped Carbons for the Design of Pt Based Oxygen Reduction Reaction Catalysts. *Carbon* **2019**, *146*, 44−59.

(2) Melke, J.; Peter, B.; Habereder, A.; Ziegler, J.; Fasel, C.; Nefedov, A.; Sezen, H.; Wöll, C.; Ehrenberg, H.; Roth, C. Metal-Support Interactions of Platinum Nanoparticles Decorated N-Doped Carbon Nanofibers for the Oxygen Reduction Reaction. *ACS Appl. Mater. Interfaces* **2016**, *8*, 82−90.

(3) Gao, S.; Fan, H.; Wei, X.; Li, L.; Bando, Y.; Golberg, D. Nitrogen-Doped Carbon with Mesopore Confinement Efficiently Enhances the Tolerance, Sensitivity, and Stability of a Pt Catalyst for the Oxygen Reduction Reaction. *Part. Part. Syst. Charact.* **2013**, *30*, 864−872.

(4) Yadav, R.; Dixit, C. K. Synthesis, Characterization and Prospective Applications of Nitrogen-Doped Graphene: A Short Review. *J. Sci.: Adv. Mater. Devices* **2017**, *2*, 141−149.

(5) Zhang, H.; An, P.; Zhou, W.; Guan, B. Y.; Zhang, P.; Dong, J.; Lou, X. W. Dynamic Traction of Lattice-Confined Platinum Atoms into Mesoporous Carbon Matrix for Hydrogen Evolution Reaction. *Sci. Adv.* **2018**, *4*, No. eaao6657.

(6) Shao, Y.; Yin, G.; Gao, Y. Understanding and Approaches for the Durability Issues of Pt-Based Catalysts for PEM Fuel Cell. *J. Power Sources* **2007**, *171*, 558−566.

(7) Groves, M. N.; Chan, A. S. W.; Malardier-Jugroot, C.; Jugroot, M. Improving Platinum Catalyst Binding Energy to Graphene through Nitrogen Doping. *Chem. Phys. Lett.* **2009**, *481*, 214−219.

(8) Yang, Y.; Gu, L.; Guo, S.; Shao, S.; Li, Z.; Sun, Y.; Hao, S. N-Doped Mesoporous Carbons: From Synthesis to Applications as Metal-Free Reduction Catalysts and Energy Storage Materials. *Front. Chem.* **2019**, *7*, No. 761.

(9) Hughes, A. E.; Haque, N.; Northey, S. A.; Giddey, S. Platinum Group Metals: A Review of Resources, Production and Usage with a Focus on Catalysts. *Resources* **2021**, *10*, No. 93.

(10) Mackus, A. J. M.; Weber, M. J.; Thissen, N. F. W.; Garcia-Alonso, D.; Vervuurt, R. H. J.; Assali, S.; Bol, A. A.; Verheijen, M. A.; Kessels, W. M. M. Atomic Layer Deposition of Pd and Pt Nanoparticles for Catalysis: On the Mechanisms of Nanoparticle Formation. *Nanotechnology* **2015**, *27*, No. 034001.

(11) Liu, C.; Wang, C. C.; Kei, C. C.; Hsueh, Y. C.; Perng, T. P. Atomic Layer Deposition of Platinum Nanoparticles on Carbon Nanotubes for Application in Proton-Exchange Membrane Fuel Cells. *Small* **2009**, *5*, 1535−1538.

(12) Wang, C. C.; Hsueh, Y. C.; Su, C. Y.; Kei, C. C.; Perng, T. P. Deposition of Uniform Pt Nanoparticles with Controllable Size on TiO2-Based Nanowires by Atomic Layer Deposition and Their Photocatalytic Properties. *Nanotechnology* **2015**, *26*, No. 254002.

(13) Zhu, Y.; Dunn, K. A.; Kaloyeros, A. E. Properties of Ultrathin Platinum Deposited by Atomic Layer Deposition for Nanoscale Copper-Metallization Schemes. *J. Mater. Res.* **2007**, *22*, 1292−1298.

(14) Karasulu, B.; Vervuurt, R. H. J.; Kessels, W. M. M.; Bol, A. A. Continuous and Ultrathin Platinum Films on Graphene Using Atomic Layer Deposition: A Combined Computational and Experimental Study. *Nanoscale* **2016**, *8*, 19829−19845.

(15) Mackus, A. J. M.; Verheijen, M. A.; Leick, N.; Bol, A. A.; Kessels, W. M. M. Influence of Oxygen Exposure on the Nucleation of Platinum Atomic Layer Deposition: Consequences for Film Growth, Nanopatterning, and Nanoparticle Synthesis. *Chem. Mater.* **2013**, *25*, 1905−1911.

(16) Lee, H. B. R.; Bent, S. F. Microstructure-Dependent Nucleation in Atomic Layer Deposition of Pt on TiO 2. *Chem. Mater.* **2012**, *24*, 279−286.

(17) Zhang, L.; Banis, M. N.; Sun, X. Single-Atom Catalysts by the Atomic Layer Deposition Technique. *Nat. Sci. Rev.* **2018**, 628−630.

(18) Yanguas-Gil, A.; Elam, J. W. Self-Limited Reaction-Diffusion in Nanostructured Substrates: Surface Coverage Dynamics and Analytic Approximations to ALD Saturation Times. *Chem. Vap. Deposition* **2012**, *18*, 46−52.

(19) Yanguas-Gil, A.*Growth and Transport in Nanostructured Materials: Reactive Transport in PVD, CVD, and ALD*, SpringerBriefs in Materials; Springer: Cham, 2017; p 128.

(20) King, J. S.; Wittstock, A.; Biener, J.; Kucheyev, S. O.; Wang, Y. M.; Baumann, T. F.; Giri, S. K.; Hamza, A. V.; Baeumer, M.; Bent, S. F. Ultralow Loading Pt Nanocatalysts Prepared by Atomic Layer Deposition on Carbon Aerogels. *Nano Lett.* **2008**, *8*, 2405−2409.

(21) Richey, N. E.; De Paula, C.; Bent, S. F. Understanding Chemical and Physical Mechanisms in Atomic Layer Deposition. *J. Chem. Phys.* **2020**, *152*, No. 040902.

(22) Hagen, D. J.; Pemble, M. E.; Karppinen, M. Atomic Layer Deposition of Metals: Precursors and Film Growth. *Appl. Phys. Rev.* **2019**, *6*, No. 041309.

(23) Cremers, V.; Puurunen, R. L.; Dendooven, J. Conformality in Atomic Layer Deposition: Current Status Overview of Analysis and Modelling. *Appl. Phys. Rev.* **2019**, *6*, No. 021302.

(24) Mackus, A. J. M.; Merkx, M. J. M.; Kessels, W. M. M. From the Bottom-Up: Toward Area-Selective Atomic Layer Deposition with High Selectivity. *Chem. Mater.* **2019**, *31*, 2−12.

(25) Aaltonen, T.; Ritala, M.; Sajavaara, T.; Keinonen, J.; Leskelä, M. Atomic Layer Deposition of Platinum Thin Films. *Chem. Mater.* **2003**, *15*, 1924−1928.

(26) Setthapun, W.; Williams, W. D.; Kim, S. M.; Feng, H.; Elam, J. W.; Rabuffetti, F. A.; Poeppelmeier, K. R.; Stair, P. C.; Stach, E. A.; Ribeiro, F. H.; et al. Genesis and Evolution of Surface Species during Pt Atomic Layer Deposition on Oxide Supports Characterized by in Situ XAFS Analysis and Water-Gas Shift Reaction. *J. Phys. Chem. C* **2010**, *114*, 9758−9771.

(27) Vervuurt, R. H. J.; Kessels, W. M. M. E.; Bol, A. A. Atomic Layer Deposition for Graphene Device Integration. *Adv. Mater. Interfaces* **2017**, *4*, No. 1700232.

(28) Yang, M.; Cheng, B.; Song, H.; Chen, X. Preparation and Electrochemical Performance of Polyaniline-Based Carbon Nanotubes as Electrode Material for Supercapacitor. *Electrochim. Acta* **2010**, *55*, 7021−7027.

(29) Kundu, S.; Xia, W.; Busser, W.; Becker, M.; Schmidt, D. A.; Havenith, M.; Muhler, M. The Formation of Nitrogen-Containing Functional Groups on Carbon Nanotube Surfaces: A Quantitative XPS and TPD Study. *Phys. Chem. Chem. Phys.* **2010**, *12*, 4351−4359.

(30) Shen, J.; Muthukumar, K.; Jeschke, H. O.; Valentí, R. Physisorption of an Organometallic Platinum Complex on Silica: An Ab Initio Study. *New J. Phys.* **2012**, *14*, No. 073040.

(31) Muthukumar, K.; Jeschke, H. O.; Valentí, R. Dynamics and Fragmentation Mechanism of $(C_5H_4CH_3)Pt(CH_3)_3$ on SiO_2 Surfaces. *Beilstein J. Nanotechnol.* **2018**, *9*, 711−720.

(32) Konh, M.; Lien, C.; Cai, X.; Wei, S. H.; Janotti, A.; Zaera, F.; Teplyakov, A. V. ToF-SIMS Investigation of the Initial Stages of MeCpPt(CH3)3 Adsorption and Decomposition on Nickel Oxide Surfaces: Exploring the Role and Location of the Ligands. *Organometallics* **2020**, *39*, 1024−1034.

(33) Mohlala, L. M.; Jen, T. C.; Olubambi, P. A. Initial Reaction Mechanism on the Atomic Layer Deposition of Platinum on a Graphene Surface: A Density Functional Theory Study. *Procedia Manuf.* **2019**, *35*, 1250−1255.

(34) Yan, H.; Lin, Y.; Wu, H.; Zhang, W.; Sun, Z.; Cheng, H.; Liu, W.; Wang, C.; Li, J.; Huang, X.; Yao, T.; et al. Bottom-up Precise Synthesis of Stable Platinum Dimers on Graphene. *Nat. Commun.* **2017**, *8*, No. 1070.

(35) Kim, K.; Lee, H. B. R.; Johnson, R. W.; Tanskanen, J. T.; Liu, N.; Kim, M. G.; Pang, C.; Ahn, C.; Bent, S. F.; Bao, Z. Selective Metal Deposition at Graphene Line Defects by Atomic Layer Deposition. *Nat. Commun.* **2014**, *5*, No. 4781.

(36) Wella, S. A.; Hamamoto, Y.; Morikawa, Y.; Hamada, I. Platinum Single-Atom Adsorption on Graphene: A Density Functional Theory Study. *Nanoscale Adv.* **2019**, *1*, 1165−1174.

(37) Durbin, D. J. D.; Malardier-Jugroot, C. Density Functional Theory Analysis of Metal/Graphene Systems as a Filter Membrane to Prevent CO Poisoning in Hydrogen Fuel Cells. *J. Phys. Chem. C* **2011**, *115*, 808−815.

https://doi.org/10.1021/acs.jpcc.2c04117
J. Phys. Chem. C 2022, 126, 16357−16368

(38) Lin, K. H.; Sun, C.; Ju, S. P.; Smith, S. C. Density Functional Theory Study on Adsorption of Pt Nanoparticle on Graphene. *Int. J. Hydrogen Energy* **2013**, *38*, 6283−6287.
(39) Wang, C. S.; Wang, H.; Wu, R.; Ragan, R. Evaluating the Stability of Single-Atom Catalysts with High Chemical Activity. *J. Phys. Chem. C* **2018**, *122*, 21919−21926.
(40) Perazzolo, V.; Brandiele, R.; Durante, C.; Zerbetto, M.; Causin, V.; Rizzi, G. A.; Cerri, I.; Granozzi, G.; Gennaro, A. Density Functional Theory (DFT) and Experimental Evidences of Metal-Support Interaction in Platinum Nanoparticles Supported on Nitrogen- and Sulfur-Doped Mesoporous Carbons: Synthesis, Activity, and Stability. *ACS Catal.* **2018**, *8*, 1122−1137.
(41) Groves, M. N.; Malardier-Jugroot, C.; Jugroot, M. Improving Platinum Catalyst Durability with a Doped Graphene Support. *J. Phys. Chem. C* **2012**, *116*, 10548−10556.
(42) Hasegawa, S.; Kunisada, Y.; Sakaguchi, N. Diffusion of a Single Platinum Atom on Light-Element-Doped Graphene. *J. Phys. Chem. C* **2017**, *121*, 17787−17795.
(43) Artyushkova, K.; Kiefer, B.; Halevi, B.; Knop-Gericke, A.; Schlogl, R.; Atanassov, P. Density Functional Theory Calculations of XPS Binding Energy Shift for Nitrogen-Containing Graphene-like Structures. *Chem. Commun.* **2013**, *49*, 2539−2541.
(44) Giannozzi, P.; Baroni, S.; Bonini, N.; Calandra, M.; Car, R.; Cavazzoni, C.; Ceresoli, D.; Chiarotti, G. L.; Cococcioni, M.; Dabo, I.; et al. QUANTUM ESPRESSO: A Modular and Open-Source Software Project for Quantum Simulations of Materials. *J. Phys. Condens. Matter* **2009**, *21*, No. 395502.
(45) Lejaeghere, K.; Bihlmayer, G.; Björkman, T.; Blaha, P.; Blügel, S.; Blum, V.; Caliste, D.; Castelli, I. E.; Clark, S. J.; Dal Corso.; et al. Reproducibility in Density Functional Theory Calculations of Solids. *Science* **2016**, *351*, No. aad3000.
(46) Prandini, G.; Marrazzo, A.; Castelli, I. E.; Mounet, N.; Marzari, N. Precision and Efficiency in Solid-State Pseudopotential Calculations. *npj Comput. Mater.* **2018**, *4*, No. aad3000.
(47) Kresse, G.; Joubert, D. From Ultrasoft Pseudopotentials to the Projector Augmented-Wave Method. *Phys. Rev. B* **1999**, *59*, 1758−1775.
(48) Blöchl, P. E. Projector Augmented-Wave Method. *Phys. Rev. B* **1994**, *50*, 17953−17979.
(49) Perdew, J. P.; Burke, K.; Ernzerhof, M. Generalized Gradient Approximation Made Simple. *Phys. Rev. Lett.* **1996**, *77*, 3865−3868.
(50) Grimme, S.; Antony, J.; Ehrlich, S.; Krieg, H. A Consistent and Accurate Ab Initio Parametrization of Density Functional Dispersion Correction (DFT-D) for the 94 Elements H-Pu. *J. Chem. Phys.* **2010**, *132*, No. 154104.
(51) Kaloni, T. P.; Cheng, Y. C.; Faccio, R.; Schwingenschlögl, U. Oxidation of Monovacancies in Graphene by Oxygen Molecules. *J. Mater. Chem.* **2011**, *21*, 18284−18288.
(52) Henkelman, G.; Uberuaga, B. P.; Jónsson, H. Climbing Image Nudged Elastic Band Method for Finding Saddle Points and Minimum Energy Paths. *J. Chem. Phys.* **2000**, *113*, 9901−9904.
(53) Momma, K.; Izumi, F. VESTA 3 for Three-Dimensional Visualization of Crystal, Volumetric and Morphology Data. *J. Appl. Crystallogr.* **2011**, *44*, 1272−1276.
(54) Cottrell, T. L. *The Strengths of Chemical Bonds*; Butterworths Scientific Publications, 1958; pp 272−288.
(55) Kessels, W. M. M.; Knoops, H. C. M.; Dielissen, S. A. F.; MacKus, A. J. M.; Van De Sanden, M. C. M. Surface Reactions during Atomic Layer Deposition of Pt Derived from Gas Phase Infrared Spectroscopy. *Appl. Phys. Lett.* **2009**, *95*, No. 013114.

https://doi.org/10.1021/acs.jpcc.2c04117
J. Phys. Chem. C 2022, 126, 16357−16368